Optimization of Lead-Free Sn-Based Perovskite Solar Cells using SCAPs-1D Simulation Techniques

Awais Maqsood , Muhammad Irfan Abid , Muhammad Kamran * , Marek Turzyński , Mehdi Tlija * , Ehab Ghith

Posted Date: 11 June 2024

doi: 10.20944/preprints202406.0524.v1

Keywords: Perovskite solar cells; Lead-free; Tin-based; SCAPs-1D Simulation and Performance opti-mization

Article

Optimization of Lead-Free Sn-Based Perovskite Solar Cells using SCAPs-1D Simulation Techniques

Awais Maqsood [1], Muhammad Irfan Abid [1], Muhammad Kamran * [2], Marek Turzynski [2], Mehdi Tlija [3] and Ehab Ghith [4]

[1] Department of Electrical Engineering and Technology, Riphah International University, Pakistan
[2] Faculty of Electrical and Control Engineering, Gdańsk University of Technology, Gdańsk, Poland
[3] Department of Industrial Engineering, College of Engineering, King Saud University, P.O. Box 800 Riyadh 11421, Saudi Arabia
[4] Department of Mechatronics, Faculty of Engineering, Ain shams University, Cairo 11566, Egypt
* Correspondence: kamran_ramzan@outlook.com

Abstract: Perovskite solar cells (PSCs) are vital for their optical and electrical properties, with lead-based PSCs reaching a remarkable efficiency of 26.1%, while tin-based counterparts achieve 18.71%. Due to lead's toxicity, there's a push for alternatives like tin. However, tin-based PSCs suffer from stability issues and high defect density states, necessitating the development of cost-effective, high-performance, and eco-friendly alternatives. In this study, we designed a hetero-junction architecture using $MASnI_3$-based Perovskite, optimized with SCAPs-1D. After exhaustive analysis, our device achieved a power conversion efficiency of 24.18%, with enhanced parameters including Voc of 0.09323V, Jsc of 30.8360 mA/cm^2, and FF of 84.10%. Recombination rates, particularly Shockley-Read Hall recombination, were significantly reduced. Parametric analyses, encompassing absorber layer thickness, band gap, defect density, doping concentration, and operating temperature, indicate potential efficiency enhancements. This underscores the viability of Sn-based PSCs as a cost-effective, efficient, and environmentally benevolent alternative to lead-based counterparts, promising advancements in future research and development efforts.

Keywords: perovskite solar cells, lead-free, tin-based, SCAPs-1D simulation and performance optimization

1. Introduction

As populations grow and living standards rise, the demand for electricity increases to power household appliances and support industrial activities [1]. To tackle the urgent issue of global warming, transitioning to renewable energy sources such as solar, hydropower, and wind are crucial for reducing pollution. However, a significant challenge with renewable energy is the need for specialized infrastructure, which is not as necessary for non-renewable sources like natural gas, coal, and oil [2, 3]. Fortunately, regions near the equator, which often require significant amounts of electricity to support higher living standards, are ideally positioned for harnessing solar energy. These areas receive consistent sunlight throughout the year, making solar energy generation highly viable [4]. The sun emits an abundance of solar energy daily, surpassing the total global energy consumption for an entire year [5].

PSCs were discovered in 2009. However, their initial energy conversion efficiency was limited to 3.8% due to the liquid electrolyte disintegrating both the electrode and the perovskite layer during operation [6]. In 2012, researchers accomplished a power conversion efficiency (PCE) of 9.7% for 500 hours, sparking renewed interest in PSCs. Figure 1 illustrates the overall setup of a PSC [7]. A transparent electrode, such as indium-tin-oxide (ITO) or fluorine-doped-tin-oxide (FTO), is coated on a glass surface, with an electron transport layer (ETL) applied on top [8]. The active perovskite layer, which absorbs photons and generates excitons, is situated above the ETL. Above the perovskite layer, a hole transport layer (HTL) is followed by a metal electrode. Together, the transparent and metal electrodes form a battery circuit [9]. Each layer in the model has been extensively researched and developed to enhance PCE by a few percent. The ETL is particularly favored because it improves electron collection and prevents electron-hole recombination, thereby increasing battery efficiency

 doi:10.20944/preprints202406.0524.v1

[10-12]. In experiments, a thick coating of TiO_2 was used, followed by a mesoporous layer to fill the pores. Without adequate TiO_2 layer thickness, efficiency decreases, and shunt resistance (Rs) increases [13]. This approach reduces electron-hole recombination and lowers ETL resistance, thus improving PCE by collecting electrons with low impedance. Various methods such as rotation, spray pyrolysis, or evaporation can be used to apply the ETL. Researchers have explored different perovskite combinations to boost the open-circuit voltage (Voc) and minimize the energy difference within the cell [14]. A broader absorption area allows more light to be absorbed, increasing the electron-hole pair generation, Voc, and overall cell energy production.

The energy gap is the difference in energy between the highest occupied molecular orbital (HOMO) and the lowest unoccupied molecular orbital (LUMO). The most frequently studied high-temperature liquid HTLs are CuSCN and Spiro Bifluorene (Spiro-OMeTAD). These HTLs are also influenced by salt and oxygen (O_2) [16]. Since Spiro-OMeTAD has low conductivity, doping is used to enhance its charge transport properties. An HTL with a heterojunction and an inherent thin layer reduces electron-hole recombination and increases the short circuit current density (JSC). Gold (Au) is considered the best metal electrode, although other metals can be used depending on the cell design [17].

This study aims to examine the microstructural characteristics of perovskite layers within solar cells, as shown in Figure 1, focusing specifically on the thickness and distribution of grain sizes. Additionally, it seeks to evaluate the chemical composition, thickness, particle size, and surface roughness of the perovskite layers and to establish a correlation between these factors and the electronic properties of the produced samples. A solar simulator may be used to evaluate the differences in energy conversion efficiency between solar panels and solar cells [18]. Quantifying the current-voltage characteristics is the test's goal. The goal of researching PSCs is the same as it is in terms of composition and production process [19]. The analysis of photoluminescence (PL) and electroluminescence (EL) investigations is significantly impacted by differences in photo-electric activity [20]. The PCE can be higher than 18% [21]. The novelty contributions of the article are as follows:

1. Introducing a novel hetero-junction architecture using $MASnI_3$-based Perovskite combined with SCAPs-1D. This innovative design demonstrates a new approach to enhancing the performance and stability of tin-based PSCs.
2. Achieving a high PCE of 24.18% through meticulous device optimization. This efficiency surpasses previous records for tin-based PSCs, showcasing the effectiveness of the proposed architecture and optimization techniques.
3. Successfully reducing recombination rates, particularly Shockley-Read Hall recombination, within the device. This advancement addresses one of the key challenges associated with tin-based PSCs, leading to improved overall performance and stability.
4. Conducting comprehensive parametric analyses covering various factors such as absorber layer thickness, band gap, defect density, doping concentration, and operating temperature. These analyses provide valuable insights into the factors influencing device performance and offer avenues for further optimization and enhancement.
5. Demonstrating the viability of tin-based PSCs as a cost-effective, efficient, and environmentally friendly alternative to lead-based counterparts. This contributes to the ongoing efforts to develop sustainable and eco-friendly photovoltaic technologies, with promising implications for future research and development endeavors.

 doi:10.20944/preprints202406.0524.v1

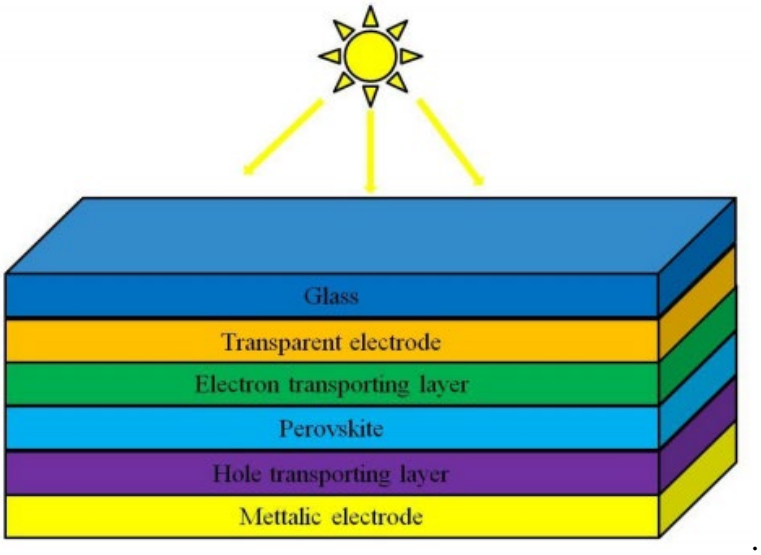

Figure 1. Illustration of the arrangement of a perovskite solar cell (PSC).

2. Materials and Methods

This section will provide comprehensive details on the device's construction as well as the particular settings used for the simulation. When constructing a Perovskite structure, three types of architecture are often used: planner (n-i-p), inverted (p-i-n), and mesoporous layouts. For our device study, we used a planner hetero-junction design based on $CH_3NH_3SnI_3$, with layers made up of FTO/ZnO/CH_3NH_3 SnI_3/CuSCN/Au. SCAP-1D, a solar cell simulator, is being used for the simulation and performance study. The Poisson equation and the equation of continuity serve as the foundation for the Gent University-developed simulation tool's operation. Using the Poisson equation (Eq. 1) [21] electron continuity equation (Eq. 2) [22], and hole continuity (Eq. 3) [23], the was solved to get performance metrics including the J-V characteristics curve, energy band diagrams, and efficiency quantum, as indicated below. Various curves are used to determine the performance characteristics of solar cells, including open circuit voltage, fill factor (FF), PCE, and short circuit current.

$$\frac{d}{dt}\left(-e(t)\frac{d\psi}{dt}\right) = q[p(t) + N_D^+(t) - N_A^-(t) + p_t(t) - n_t(t)] \quad (1)$$

$$\frac{dP_n}{dy} = G_p - \frac{P_n - P_{n0}}{\tau_p} + p_n\mu_p\frac{d\xi}{dy} + \mu_p\xi\frac{dP_n}{dy} + D_p\frac{d^2P_n}{dy^2} \quad (2)$$

$$\frac{dn_p}{dy} = G_n - \frac{n_p - n_{p0}}{\tau_n} + n_p\mu_n\frac{d\xi}{dy} + \mu_n\xi\frac{dn_p}{dy} + D_n\frac{d^2n_p}{dy^2} \quad (3)$$

Where e (t) is the electrostatic constant, ψ is electrostatic potential, q is electric charge, p (t) is the density of holes, $N_D^+(t)$ is the density of ionized acceptor impurities, $\boldsymbol{N_A^-(t)}$ is the density of ionized donor impurities, $\boldsymbol{p_t(t)}$ is the density of photogenerated holes, and $\boldsymbol{n_t(t)}$ is the density of photogenerated electrons. P_n is the electron density, G_p is the generation rate of electron-hole pairs due to absorption of light or other external stimuli, Pn0 is the equilibrium electron density, τ_p is carrier lifetime, representing the average time a carrier (electron or hole) remains in the semiconductor before recombination, μ_p is hole mobility, indicating how fast holes move under the influence of an electric field, $\boldsymbol{\xi}$ is dimensionless recombination rate, D_p is hole diffusion coefficient, representing how holes spread out in space due to random thermal motion, n_p is hole density, G_n is generation rate of electron-hole pairs due to absorption of light or other external stimuli, n_{po} is equilibrium hole density, τ_n is carrier lifetime, representing the average time an electron remains in the semiconductor

 doi:10.20944/preprints202406.0524.v1

before recombination, μ_n is electron mobility, indicating how fast electrons move under the influence of an electric field, D_n is electron diffusion coefficient, representing how electrons spread out in space due to random thermal motion.

A system's generation rate (G), hole lifetime, electron lifetime, diffusion coefficient, electron charge, electrostatic potential, hole mobility, electron mobility, the concentration of free electrons, the concentration of trapped electrons, concentration of ionized acceptor concentrations, ionized donor concentrations, electric field, and thickness (represented by x) are among the parameters that are used to determine various aspects of a system. Figure 2 shows the whole device construction, including all the temporary layers. The HTL is Cu_2O, the ETL is TiO_2, the absorber layer is $MASnI_3$, the rear metal contact is Au, and the front metal contact is FTO. The FTO & ETL interface, ETL & Perovskite interface, and Perovskite & HTL interface are the three basic interfacing layers that make up the Perovskite device. The results and simulations are carried out under standard testing conditions, with an air mass of AM 1.5 G, a temperature of 300 K, and an illumination intensity of 1000 W/m^2.

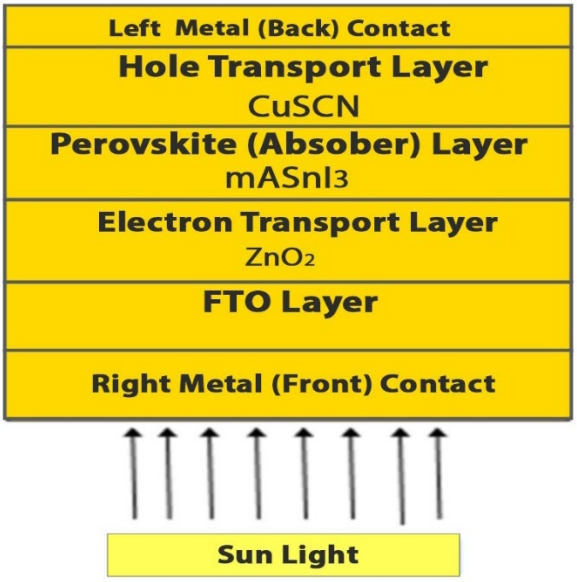

Figure 2. Illustration of the n-i-p planar layout, showcasing the comprehensive coverage of each layer in the device's design.

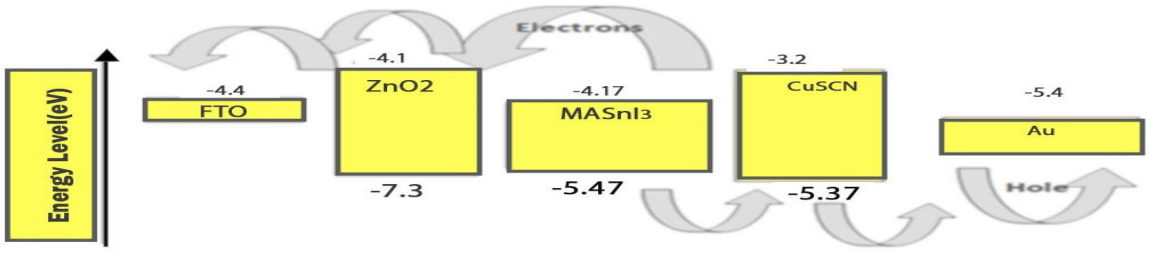

Figure 3. Diagram depicting the energy levels in a perovskite device.

Tracing the movement of electrons and holes emitted from the absorber layer has demonstrated the energy level representation in Figure 3. In this PSC diagram, the energy levels are marked by specific numerical values in electron volts (eV) which indicate the potential energy of electrons within the materials. The Fluorine-doped Tin Oxide (FTO) has an energy level of -4.4 eV, acting as the front electrode. The Titanium Dioxide (TiO_2), a semiconductor material, has a conduction band at -4.1 eV, which is energetically favorable for accepting electrons from the perovskite layer, whose conduction band is at -4.17 eV. These excited electrons move from the perovskite to the TiO_2 and then to the FTO,

 doi:10.20944/preprints202406.0524.v1

contributing to the current. On the hole transport side, the Cuprous Oxide (Cu_2O) has its conduction band at -3.2 eV and its valence band at -5.37 eV. The holes, with a higher energy level in the perovskite layer (-5.47 eV), migrate towards the Cu_2O layer and then to the Gold (Au) electrode, which has an energy level of -5.4 eV. This energy alignment allows for efficient hole transport to the Au electrode, thereby completing the circuit within the solar cell for electricity generation. These precise energy level values are critical for the design and functionality of the cell, dictating the charge transfer processes and influencing the overall efficiency of the device. Furthermore, all of the device's layers have had their valence band (VB) and conduction band (CB) values evaluated.

2.1. CuSCN-oriented HTL

In organic optoelectronic devices, Copper-thiocyanate (CuSCN) is widely used as a hole-transport layer. However, due to its coordination polymer structure, the processing of its solution is difficult. The traditional process requires solvents based on sulfides that have a strong affinity for copper. We propose a simple solution to this issue, which is to rinse the CuSCN hole-transport layer with anti-solvents such as acetone or tetrahydrofuran [24]. The effectiveness of this treatment has shown promising results in raising the efficiency of organic light-emitting diodes and solar cells that use CuSCN at HTL as a component. By applying this anti-solvent treatment, we can significantly raise the organic photovoltaic system's Jsc and FF.

When cells treated with acetone or tetrahydrofuran are used, the mean PCE of optical PV devices using untreated CuSCN may be raised from 8.18% to 9.16% and 9.25%, respectively. Furthermore, the external quantum efficiency of organic light-emitting diodes with CuSCN HTL is improved by the use of tetrahydrofuran treatment, rising from 5.2% to 8.2%. The simple use of anti-solvent treatment provides an excellent method for enhancing CuSCN solution processing in various organic optoelectronic devices. Manufacturers can expect improved device performance and efficiency by incorporating this technology into the manufacturing process. The next steps would be to carry out more research and development to improve the anti-solvent treatment procedure, look at alternative anti-solvents, and assess how well they work with different device designs.

For Perovskite solar cells, the traditional method of synthesizing HTL, CuSCN on an Indium-doped Tin Oxide (ITO) substrate is costly and time-consuming. It is suggested that Mono ethanol amide (MEA) be used as the only solvent in the CuSCN layer manufacturing process. A two-step spin coating process and a low-temperature annealing process will be used to accomplish this. To get a similar HTL result for Perovskite solar cells, MEA may be used as a solvent, which lowers the manufacturing time and cost. SEM, X-ray diffraction (XRD) [28], and ultraviolet-visible spectroscopy (UV-Vis) were used to evaluate the surface morphology, crystallinity, and optical characteristics of the CuSCN layer, respectively. I-V measurements were used to calculate the layer's resistivity. Carefully selected for optimal efficiency, a temperature of 100 °C produced a perfect structure and 77.30 S/m of conductivity. By employing MEA as a solvent in this innovative way, HTL layers may be produced more quickly, easily, and affordably, which lowers the overall cost of producing solar cells [25]. Through the appropriate combination of solvent and annealing temperature, the researchers have discovered a more economical and productive method for producing HTL layers. This innovation might have a big effect on the solar cell market as it streamlines the procedure and lowers expenses. It makes it possible to produce HTL layers in large quantities, which lowers the cost and increases accessibility to the manufacture of solar cells. To guarantee consistent outcomes on a bigger scale, more optimization and scalability studies are required in the following stages. Further research and application of MEA will depend critically on examining its long-term stability as well as its compatibility with other materials.

2.2. ETL based on ZnO

PSCs possess immense potential for widespread utilization due to their low processing temperature and high mobility. However, the instability of Perovskite layers atop ZnO has hindered their broad adoption, resulting in subpar device performance. To tackle this issue, a novel approach is proposed, incorporating a bilayer of Y-doped TiO_2 and V-doped ZnO for electron transport.

 doi:10.20944/preprints202406.0524.v1

Significant enhancements in the performance of PSCs are achieved by introducing extrinsic doping of TiO_2 with Yttrium and utilizing V-doped ZnO as an ETL with precisely calibrated doping levels. Compared to solar cells utilizing pure ZnO-based ETLs, which attain a PCE of 9.4%, the photovoltaic cell employing the (V ZnO/YTi) bilayer ETL achieves the highest PCE of 15.1%. This device demonstrates a FF of 74%, a Voc of 923 mV, and a Jsc of 22 mA/m^2, showcasing the improved electron transport facilitated by the bilayer structure of the ETL [26]. By addressing the instability issues associated with ZnO-based ETLs, this innovative approach opens avenues for the widespread adoption of PSCs. Further efforts to expand and refine the (V ZnO/$YTiO_2$) bilayer ETL for commercial manufacturing can lead to wider acceptance and utilization of Perovskite solar cells. This bilayer ETL offers a solution to the challenges posed by the instability of Perovskite layers deposited atop ZnO, thereby enhancing the performance and stability of PSCs.

2.3. FTO Glass Coating

On a large scale, organic and inorganic PSCs show promise as a cost-effective alternative for photovoltaic systems. However, these cells are still vulnerable to issues with deterioration and concerns over the toxicity of the lead used in their production. Therefore, finding effective ways to handle PSC waste and recycle its components is essential. This work aims to recycle this expensive component present in the construction of mesoporous planar PSCs by introducing a systematic procedure for removing the fluorine-doped tin oxide-coated glass substrate step-by-step. By methodically eliminating each layer, this procedure makes it easier to preserve the chemical characteristics of specific components, such as gold and Spiro-OMeTAD. As a result, reusing the material is easier. Moreover, it ensures that the dangerous Pb element will be separated without contaminating other materials [27]. After all layers are removed completely, FTO conductive glass is recovered and can be used for a variety of purposes outside of photovoltaics. Comparing recycled FTO glasses with commercial glasses revealed little variations in their electrical, morphological, and physical properties. This attests to the recycling method's effectiveness in recovering the substrate while preserving its physicochemical characteristics.

The recommended method of layer-by-layer extraction of PSC waste offers a workable and environmentally responsible way to handle PSC waste at the end of its useful life [28]. By permitting the reusing of priceless components and mitigating the danger of lead contamination, this approach successfully addresses the issues surrounding the degradation and toxicity of PSC technology. When taking expected value into account, recycling FTO-coated glass substrates significantly reduces the cost of producing new substrate materials for PSCs. This lowers the environmental impact associated with the extraction and manufacture of raw materials and increases the overall cost-effectiveness of solar equipment. The solar energy industry's sustainability may be greatly increased by putting this recycling technique into practice [29]. It promotes the reuse of valuable resources and reduces waste, which helps to move towards a circular economy. It should be the top priority of future research and development projects to improve and broaden this recycling method. The next steps entail looking at other applications for recycled FTO conductive glass outside of its present purview in a variety of sectors. Solar energy. This recycling technique will also be further validated by long-term experiments that assess the durability and performance of recycled components in real-world settings.

 doi:10.20944/preprints202406.0524.v1

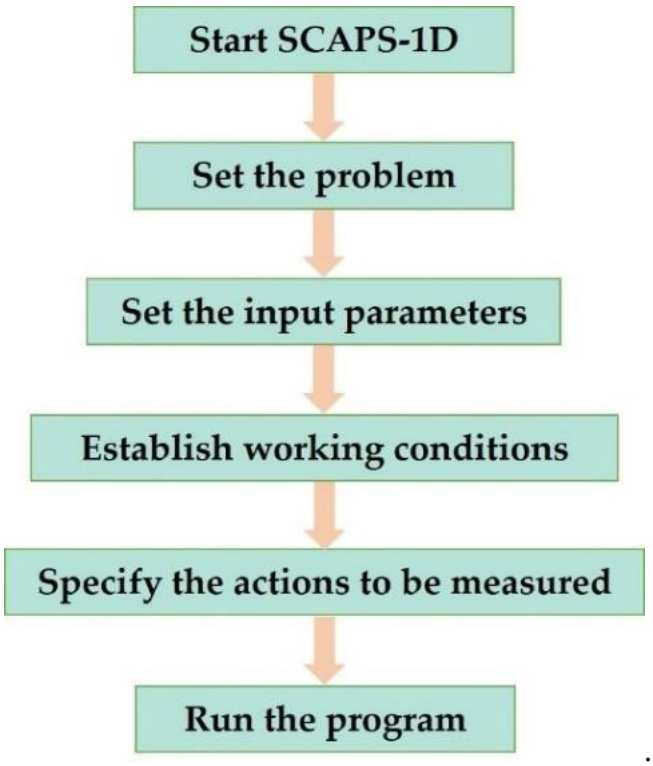

Figure 4. Steps for constructing and simulating a solar cell using SCAPS-1D.

Ensuring the purity of FTO layers on glass substrates during recycling is crucial. To verify that the recycling method is effective in recreating pristine FTO glass substrates without affecting the crystal arrangement or corroding the conductive oxide layer, X-ray diffraction research was conducted on both the recycled and reference substrates. X-ray diffraction analysis was used to demonstrate the effectiveness of the recycling process since the diffract grams of the recycled and reference FTO glasses were identical. The absence of any new peaks or alterations in their positions indicates that the conductive oxide layer and crystal structure remained intact. The results of the XRD examination showed that the fresh FTO's peak intensity was lower than the recycled FTO's [30]. The effect of particle size distributions, where the full-width half maximum shows an inverse connection with the crystallite size, may be responsible for this phenomenon.

The greatest drop in the whole breadth half causes the area of the peak to expand as the crystallite's size increases. Diffractometer factors, such as differences in the 'time per phase' parameters or the bi-oxidation status in some samples due to high-temperature annealing, may also impact the discrepancy in peak intensity. It is vital to look at the XRD pattern of FTO that still has an intact TiO_2 mesoporous layer to fully confirm the lack of TiO_2 in the recycled foundation. Additional evidence of the recycled substrate's purity would come from the absence of recognizable TiO_2 spikes in its phase.

2.4. SCAPS-ID

The simulation program SCAPs-1D developed by the IMEC research institute in Belgium, is capable of modeling and analyzing solar devices with accuracy. In particular, attention is drawn to SCAPs-1D, a simulation program that only permits the rear to be excluded as input. Improving SCAPs-1D software by allowing the back to be included as an input parameter is the suggested fix. With this enhancement, photovoltaic device simulations and analyses will be more thorough.

 doi:10.20944/preprints202406.0524.v1

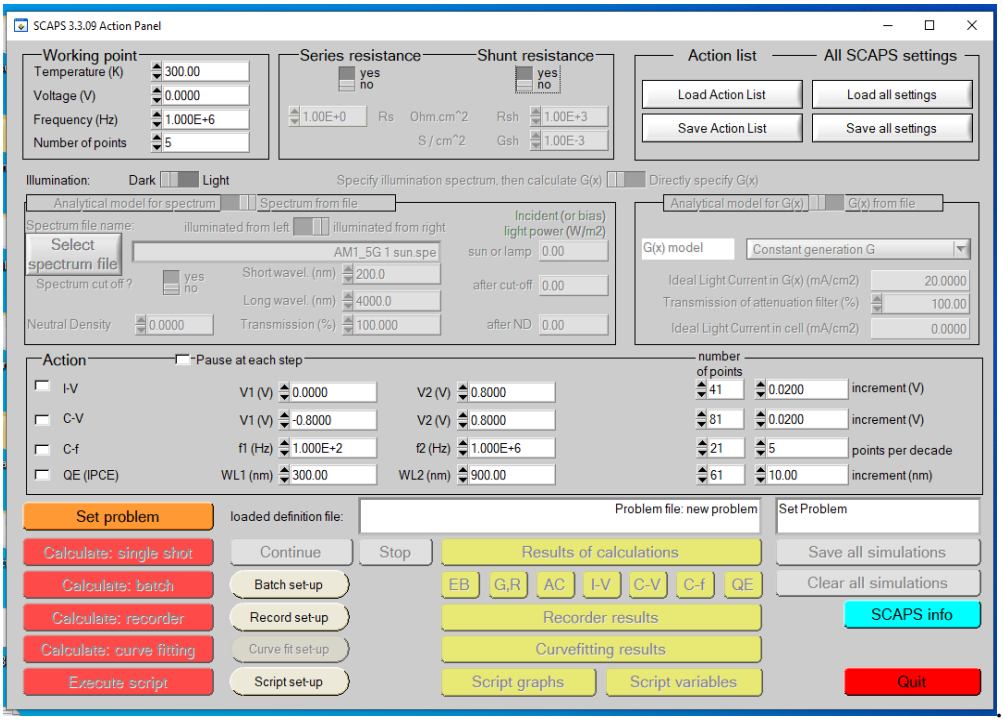

Figure 5. SCAPS 3.3.09 Action Panel.

Researchers and users of SCAPs-1D software will benefit from a more reliable and accurate simulation experience thanks to the implementation of this update [31]. Figure 3 shows that better optimization and assessment of solar cell architectures will be possible with the capacity to take the back into account as an input, resulting in more accurate predictions of device behavior. This improvement has a substantial impact as it broadens the scope of SCAPs-1D software and makes it easier for researchers to gain a deeper understanding of the optical and electrical properties of materials. As a result, this advances the understanding and practical optimization of solar devices. The next steps involve incorporating the enhancement into the existing SCAPs software framework, ensuring that it is compatible with Windows. Furthermore, it is critical to offer easily navigable documentation and instructions to guarantee simple access to and usage of the enhanced SCAPs-1D program. SCAPs-1D simulation for numerical structural property modeling of semiconductors. Regarding process simulation, Figure 4 shows the steps that must be followed to build and simulate the recommended equipment, and the action plane by the SCAPs-1D is shown in Figure 5

Table 1. Simulation parameters for each layer of a perovskite device.

Parameters	FTO	ZnO	$CH_3NH_3SnI_3$	CuSCN
Thickness (nm)	400	50	650	150
Electron affinity(eV)	4.00	4.200	4.170	2.200
Bandgap(eV)	3.500	3.260	1.350	3.400
CB effective density (cm^{-3})	2.2×10^{18}	2.2×10^{18}	2.2×10^{18}	1.7×10^{19}
Dielectric permittivity (Er)	9.000	10.000	8.200	10.000
VB effective density state (cm^{-3})	1.8×10^{18}	1.8×10^{18}	1.8×10^{18}	2.5×10^{21}
Hole mobility up (cm^2/Vs)	1.0×10^{1}	1.0×10^{7}	3.0×10^{2}	1.0×10^{-1}
Thermal velocity of Hole (cm/s)	1.0×10^{7}	1.0×10^{7}	1.0×10^{7}	1.0×10^{7}
Thermal velocity of Electron (cm/s)	2.0×10^{1}	1.0×10^{7}	1.0×10^{7}	1.0×10^{7}
Acceptor density NA (cm^{-3})	0.0×10^{0}	0.0×10^{0}	1.0×10^{1}	1.0×10^{18}
Donor density ND(cm^{-3})	1.0×10^{19}	1.0×10^{17}	0.0×10^{0}	0.0×10^{0}
Density of Defect NA (cm^3)	1.0×10^{15}	1.0×10^{15}	1.0×10^{15}	1.0×10^{15}

 doi:10.20944/preprints202406.0524.v1

3. Result and Discussion

3.1. Impact of absorber layer thickness on performance parameters

The thickness of the absorber layer is critical for improving the performance of PSC devices. Choose the absorber layer's thickness carefully to guarantee maximum absorption capacity and carrier diffusion length. The study investigated how changing the thickness of the absorber layer between 300 nm and 1000 nm affected the device's performance. The computations' outcomes are displayed in Figures 6 (b) and (c) the graphs show that increasing the thickness of the material resulted in significant enhancements in both Jsc and PCE values. The increase occurred between 300 nm to 900 nm due to improvements in the absorption coefficient, as shown in prior studies [32].

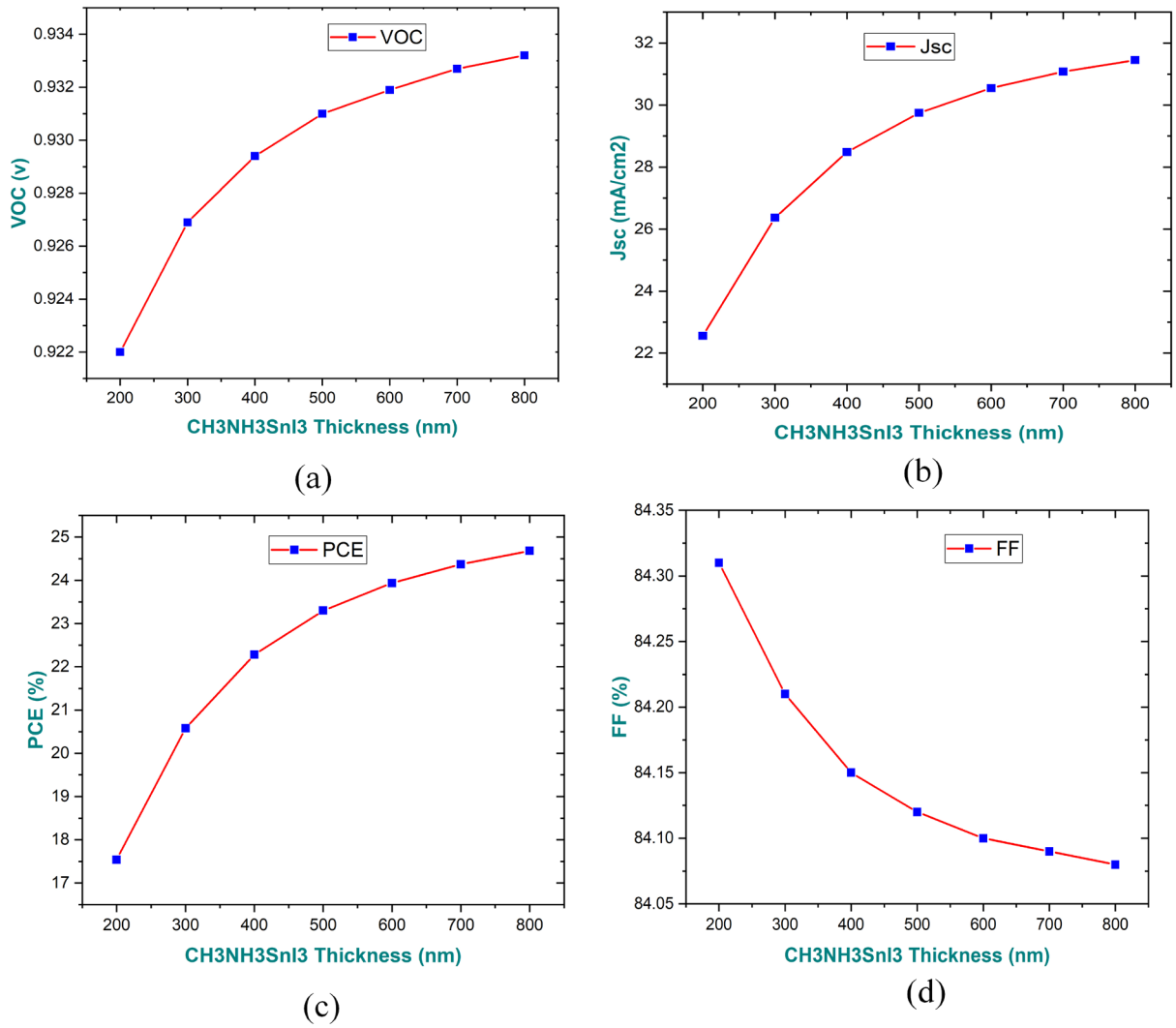

Figure 6. Impact of Thickness on performance parameters of $CH_3NH_3SnI_3$ (a) Voc (b) Jsc (c) PCE (d) FF**.**

The Voc value decreased with an increase in absorber thickness due to a notable rise in the recombination charge rate across the absorber layer generated by the thicker layer [28] shown in Figure 6 (a). The reduction in the FF value coincided with the rise in thickness of the absorber layer shown in Figure 6 (d). The increased thickness of the absorber layer results in higher series resistance in the device. The PCE increased from a wavelength of 300 nm to 800 nm but then decreased significantly. The reduction in PCE as thickness decreases is due to a decrease in carrier diffusion length. This reduction in diffusion length is especially notable within the 300 nm to 800 nm region.

 doi:10.20944/preprints202406.0524.v1

On the other hand, if the thickness exceeds 800 nm, it causes a significant decrease in carrier diffusion length and increases recombination rates, ultimately degrading the PCE [33].

Figure 6 (a), (b), (c), and (d) present the performance characteristics of PSCs at varying thickness levels, measured in nanometers (nm). As the thickness increases from 350 nm to 600 nm, there is a steady rise in the Voc from 0.72V to 0.93V. However, beyond 600 nm, Voc begins to plateau or slightly decrease. The Jsc shows a modest increase from 26.39 $mAcm^{-2}$ at 350 nm to 30.83 $mAcm^{-2}$ at 600 nm, before stabilizing or experiencing minor fluctuations. The FF exhibits variability across thickness levels but generally falls within the 75-85% range. PCE, meanwhile, fluctuates across different thicknesses, reaching its peak of 24.18% at 600 nm, with values ranging from 18.03% to 24.18% across the tested thicknesses. These findings suggest the presence of an optimal thickness range for maximizing PCE, with further investigation warranted to understand the underlying factors influencing PSC performance beyond this range.

3.2 . *Impact on doping concentration (NA) of absorber layer on the parameters of performance*

The effectiveness of Perovskite can be compromised by the acceptor density of holes within the absorbent layer. Sn-based Perovskite is particularly prone to high instability in the presence of air, which can lead to a change in its oxidation state from Sn^{2+} to Sn^{4+} due to self-p-type dopants. This oxidation process significantly impacts the efficiency of tin-based Perovskite devices. Takashi and his team proposed altering the hole concentration up to 1.0 x 1010 cm^{-3} to evaluate its effect on performance metrics.

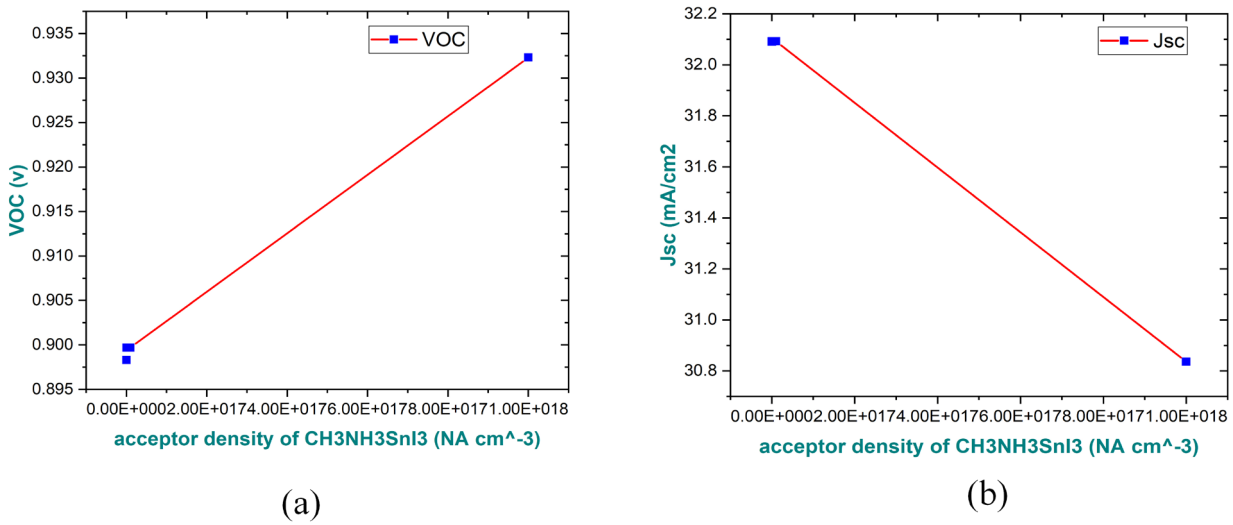

Figure 7. Impact on doping concentration (NA) of $CH_3NH_3SnI_3$.

The acceptor density (NA) was systematically varied from 1.0 x 10^{13} to 1.0 x 10^{16} cm^{-3}, and the results are depicted in Figure 7. Increasing doping concentration (NA) values enhances the Voc of the Perovskite. This is attributed to a decrease in the Fermi-energy levels of holes and an increase in the built-in biased voltage (Vbi). However, higher doping concentrations lead to a slight reduction in Jsc values due to an increased likelihood of significant recombination rates. Accepter density values ranging from 1.0 x 10^{13} to 1.0 x 10^{15} in the absorber layer resulted in noticeable improvements in FF and PCE, as shown in Figure 7(a) and (b). These improvements stem from the longer carrier diffusion length and lower resistance of the Perovskite structure.

3.3. *Impact on absorber layer defect-density NA on parameters the performance*

Tin-based Perovskites exhibit high sensitivity to defects, with their performance and stability predominantly determined by the defect density within the absorber layer. Defects can manifest as

Preprints.org (www.preprints.org) | NOT PEER-REVIEWED | Posted: 11 June 2024 doi:10.20944/preprints202406.0524.v1

bulk flaws within the PSC or as interfacial defects between the layers of the PSC and their corresponding carrier layers. These flaws are often present at the surface boundaries and contribute to the creation of shallow energy levels in the Perovskite's energy band diagram, as illustrated in Figure 3.

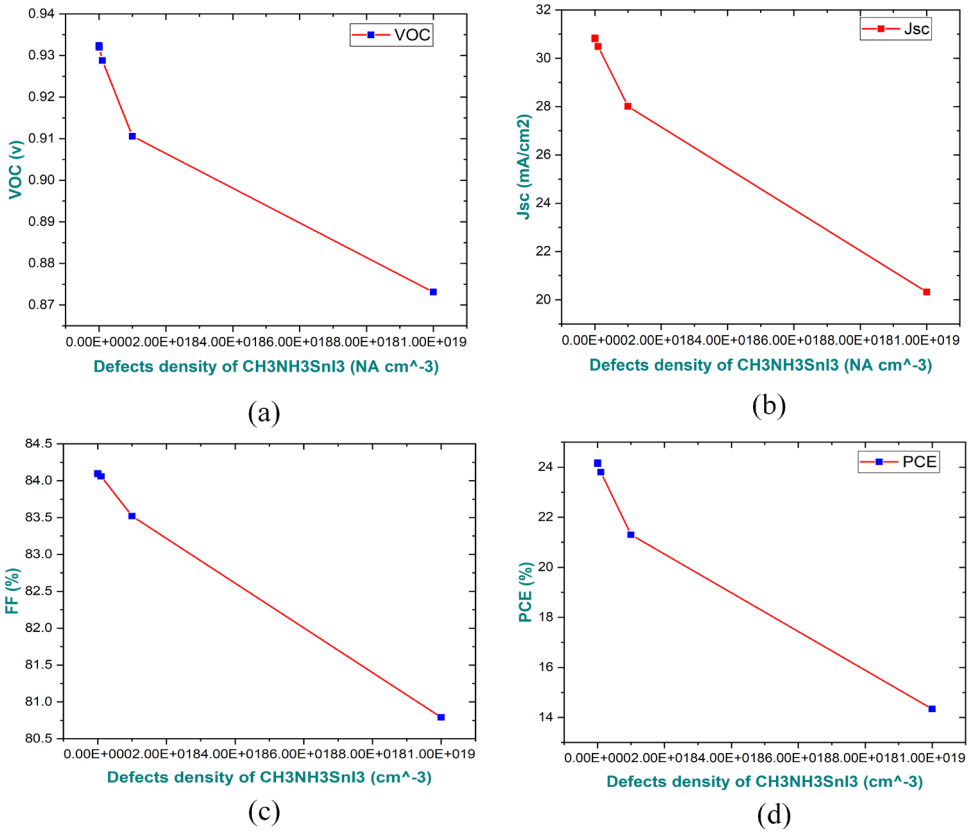

Figure 8. Impact on defects density of $CH_3NH_3SnI_3$ (a) Voc (b) Jsc (c) FF (d) PCE

The diffusion length of charges within perovskite materials is significantly affected by the density of defects in the absorber layer. Higher levels of structural defects in the perovskite structure result in shorter diffusion lengths for charge carriers. To assess the impact of increased defect density in the absorber layer on performance metrics, the defect density was varied from $1x10^{13}$ to $1x10^{19}$ cm^{-3}. The results, summarized in Table 1, clearly show that higher defect densities lead to declines in various performance indicators such as Voc, Jsc, FF, and PCE, as illustrated in Figure 8 parts (a), (b), (c), and (d). This decrease is attributed to the reduced carrier diffusion length caused by higher defect densities. At the highest tested defect density of $1x10^{19}$ cm^{-3}, the device showed significant performance degradation and was considered unstable. The Shockley-Read-Hall recombination model is useful for analyzing the effect of defect density on the absorber layer. Perovskite typically exhibits three types of recombination currents: radiative, non-radiative, and Auger. The non-radiative currents, governed by the Shockley-Read-Hall mechanism, are especially sensitive to high defect densities in the absorber layer. The recombination rate in perovskite is directly proportional to the defect density, which significantly contributes to the reduced performance of perovskite solar cells. Interfacial defects within the perovskite device are largely affected by the conduction band offset (CBO) value between the absorber layer and the buffer layer. To mitigate interfacial defects, it is beneficial to adjust the CBO values from negative to positive by integrating appropriate interfacial layers between the absorber and the respective transport layers. The ETL of the perovskite shows more interfacial defects compared to the interface between the perovskite and the HTL. The carrier diffusion length, dictated by the defect density in the absorber layer, can be analytically estimated using Equation (4).

$$L_D = \sqrt{D\tau} \qquad (4)$$

 doi:10.20944/preprints202406.0524.v1

The carrier diffusion length constant, D, is directly proportional to the movement of electron and hole charges. The increased defect density in the absorbent layer is believed to be a key reason behind the reduced carrier diffusion width and subsequent underperformance of the Perovskite device. A decreased defect density in the absorber layer at a concentration of $1x10^{13}$ cm^{-3} led to reduced recombination current and increased carrier diffusion length, ultimately improving performance characteristics.

3.4. Interfacing defects state Analysis between ETL/Perovskite

The preceding section discussed the influence of absorber layer defect density in-depth, presenting tentative conclusions and causes for the performance decline of Perovskite. We utilized planner architecture (n-i-p) in our modeling and design to create a $MASnI_3$-based Perovskite. In planner designs, there is more carrier mobility for holes created in the absorber layer to go towards the corresponding HTL and electrodes compared to electrons. Understanding planner designs is crucial for analyzing interfacial flaws between ETL/Perovskite interfaces because of the significant recombination current present.

Assessing the influence of interfacial defects between the ETL and Perovskite is important due to the reduced electron mobility towards the electrodes. The study examined how varying interfacial defect densities between $1x10^{16}$ to $1x10^{19}$ cm^{-2} affected performance parameters. The study discovered that raising the density of absorber imperfections negatively impacted performance measures. Increasing the amount of interface flaws resulted in a significant reduction in all performance measures. The drop in Jsc values is due to the large Shockley-Read-Hall (SRH) combination current at the interface between the Perovskite and ETL. Another reason causing the decrease in Voc values is the presence of dark saturation current, which significantly reduces the open circuit voltage of Perovskite. The dark saturation current increases as the recombination current also rises. The connection between Voc and reverse saturation current may be found using Eq. (5)

$$V_{oc} = \frac{nKT}{q} ln\left(\frac{J_{sc}}{J_0}+1\right) \quad (5)$$

In the equation provided, the variables n, T, q, J_{SC}, J_o, and V_{OC} correspond to the ideality factor, temperature, charge, open-circuit voltage, reverse saturation current, and open-circuit voltage, respectively, as indicated in Figures 9(a), (b), and (c). An increase in recombination current leads to a rise in the reverse saturation current, which consequently decreases the value of V_{OC}, as depicted in Figure 9.

Preprints.org (www.preprints.org) | NOT PEER-REVIEWED | Posted: 11 June 2024 doi:10.20944/preprints202406.0524.v1

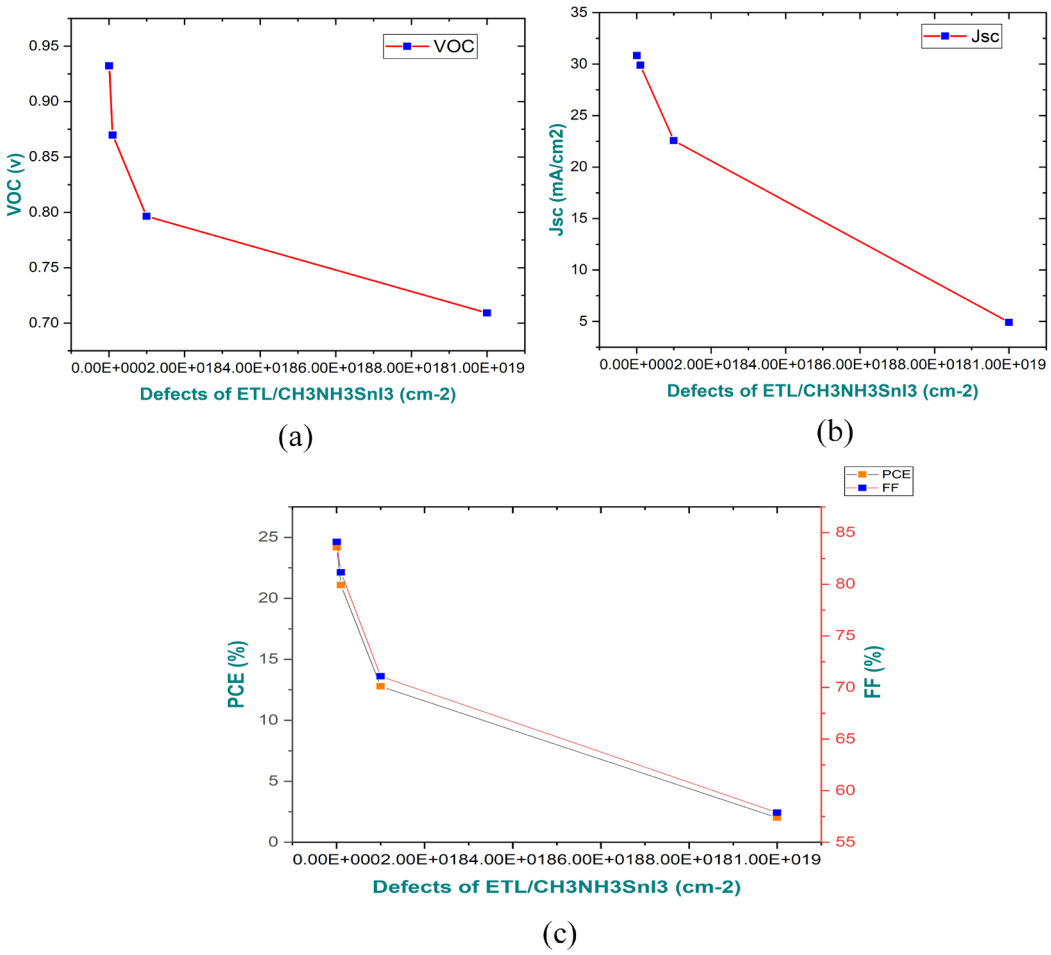

Figure 9. Impact of interfacing Defects density (NA) of ETL/CHENH$_3$SnI$_3$ (a) V_{OC} (b) J_{sc} (c) FF (d) PCE

3.5. Impact of the band gap of the Absorber layer on the performance parameters

The band gap values of Sn-based Perovskite vary depending on the kind of Perovskite and the halides substituted. The band gap of the material ranges from 1.3 eV to 2.15 eV, as reported in reference [35]. We altered the band gap of MASnI$_3$-based Perovskite in our simulation from 1.30 eV to 1.44 eV to assess its impact on the device's performance parameter. An increase in the band gap values of Perovskite J_{SC} led to a decrease in the FF and PCE performance values. If the sole metric that rose was V_{OC}, it was due to an increase in band gap values. The increase in V_{OC} was due to a direct correlation between band gap and V_{OC} values. As the band gap increased, the radiative recombination rate decreased, leading to better V_{OC} values.

Large band gap values result in poorer J_{SC} values due to the reduced production of electrons from the absorber layer. The deterioration of the FF occurred because of a mismatch in band gap alignment between the HTL and the absorber layer. Similar patterns were seen in the deterioration of PCE, which is mostly dependent on FF and tends to decline as the FF value decreases. The highest performance of the Perovskite device was attained with a band gap value of 1.35 eV, which is closely aligned with existing literature and published research [36-39].

Preprints.org (www.preprints.org) | NOT PEER-REVIEWED | Posted: 11 June 2024 doi:10.20944/preprints202406.0524.v1

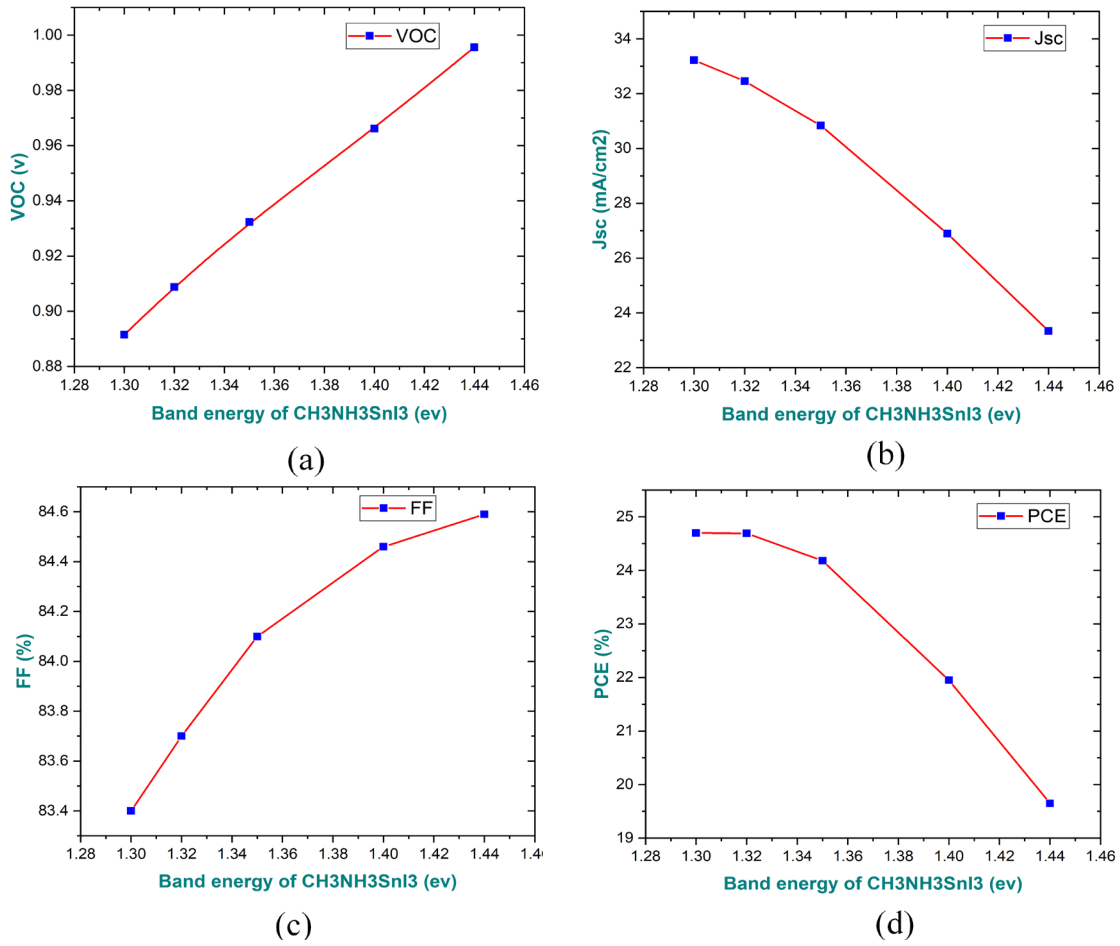

Figure 10. Impact of energy band on the $CH_3NH_3SnI_3$ performance parameters are (a) Voc (b) Jsc (c) FF (d) PCE

3.6. Impact of Temperature on performance parameters of the device

Fluctuations in operating temperature significantly impact the performance of PSCs [37]. We maintained the operating temperature at 300K for ideal circumstances in our modeling and design work. The impact of operating temperature on the performance of the Perovskite device was investigated by varying the temperature from 300K to 500K, and the findings are presented in Figure 11. Increasing the temperature considerably decreased the Voc, FF, and PCE. The decline in Perovskite performance metrics with increasing temperature is attributed to changes in carrier concentrations, charge carrier mobility, device resistance, and band gap [38, 39]. Increased temperature can lead to more stress and deformation in Perovskite devices, leading to increased interfacial recombination and SHR current transformation. Another factor contributing to decreased performance is the reduced carrier diffusion length and elevated resistance of the Perovskite device caused by recombination current (Shockley-Read-Hall and interfacial), leading to a decrease in Figure 11 (a),(b),(c), and (d) show the FF and PCE. The decrease in J_{sc} was caused by enhanced band gap values resulting from an increase in temperature [40]. The decrease in V_{OC} was caused by an increase in the dark saturation current (J_o), which leads to electron instability at higher temperatures.

Preprints.org (www.preprints.org) | NOT PEER-REVIEWED | Posted: 11 June 2024 doi:10.20944/preprints202406.0524.v1

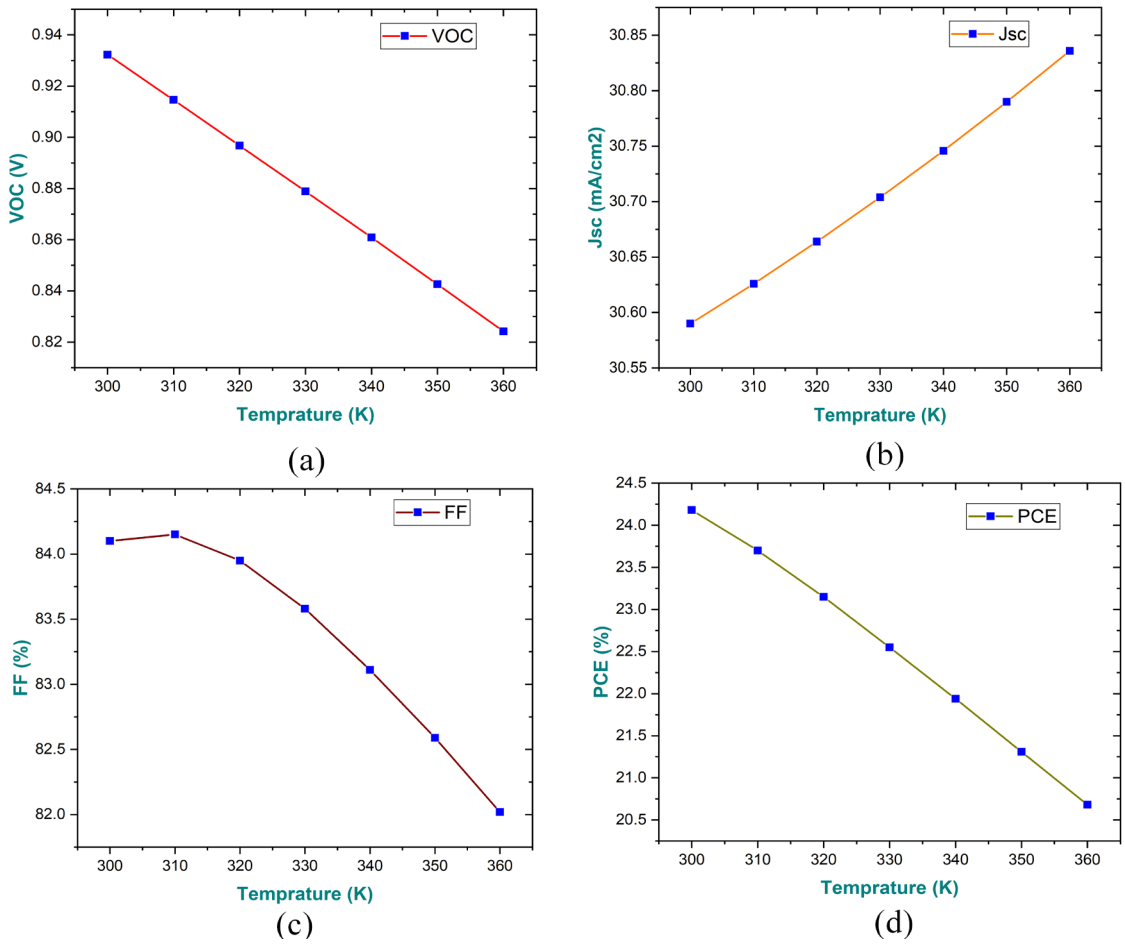

Figure 11. Temperature impact on $CH_3NH_3SnI_3$ (a) V_{OC} (b) J_{sc} (c) FF (d) PCE

Figure 11 provides data on the performance of PSCs at different temperatures, ranging from 300 K to 360 K. As the temperature increases, there is a notable decrease in the V_{OC}, dropping from 0.80V at 320 K to 0.38V at 360 K. This trend suggests that higher temperatures negatively impact the ability of the solar cell to maintain voltage in the absence of an external load. Conversely, the J_{SC} remains constant at approximately 30.03 $mAcm^{-2}$ across all temperature levels, indicating that the amount of current produced by the solar cell under short-circuit conditions is unaffected by temperature variations. However, the FF and PCE show a significant decline as temperature rises. At 320 K, the FF is 77.17%, but it decreases to 6.69% at 360 K, suggesting that higher temperatures lead to increased losses within the solar cell's internal circuitry. Consequently, PCE drops from 18.67% at 320 K to 6.69% at 360 K, indicating the adverse impact of elevated temperatures on overall solar cell performance. These results underscore the importance of temperature management strategies in optimizing the efficiency and reliability of PSCs for practical applications.

3.7. Impact on Electron Affinity of ETL on the performance of the parameter

The efficiency of perovskite devices is sensitive to variations in electron affinity within the ETL and HTL. The electron affinity values of both the HTL and ETL are crucial for determining the band gap alignment with the perovskite material.

 doi:10.20944/preprints202406.0524.v1

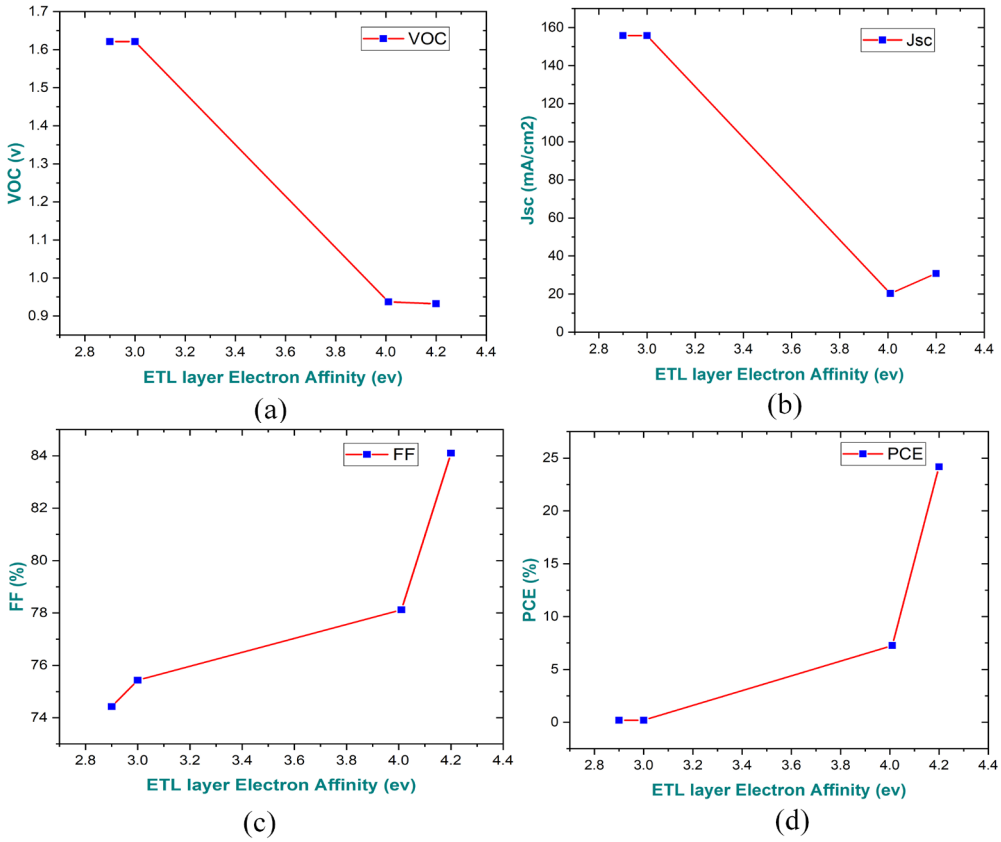

Figure.12 Impact on electron affinity of ETL (a) Voc (b) Jsc (c) FF (d) PCE

Furthermore, the usefulness of Perovskite may be negotiated by a mismatch in band gap alignment resulting from varying electron affinity values between the ETL and HTL. This disparity makes a boundary that hinders the movement of charges. In our simulations, we examined various levels of electron affinity for the ETL (ranging from 3.9 to 4.2 eV) and HTL (ranging from 2.8 to 3.4 eV) to assess their impact on device performance.

Varying the electron affinity values of the ETL from 3.9 ev to 4.2 ev significantly improved performance indicators including FF, Voc, and PCE in Figure 12 (a),(b),(c) and (d) The enhancement is due to the heightened electron mobility from the absorber layer to the ETL. When the electron affinity value surpasses 4.2 eV, the performance characteristics decline because of a band gap misalignment between the Perovskite and ETL, leading to structural instability. The electron affinity values of HTL followed a similar trend, showing enhanced outcomes when the values were increased from 2.8 to 3.4. This enhancement is due to the improved movement of holes from the absorber layer to the corresponding HTL.

3.8. Impact of Series (Rs) & Shunt Resistance (Rsh) on performance parameters

This section examines the influence of Rs and Rsh on the performance characteristics of Perovskite. It is important to consider the series and shunt resistance in real circumstances since they significantly impact the device's performance. The influence of Rs & Rsh was examined by varying parametric values and computing the results as shown in the table below. When the series resistance was adjusted between 1 and 6 ohms.cm^2, the FF and PCE of the Perovskite solar cell decreased significantly. PCE degradation increased with series resistance due to a decrease in FF values, as FF is directly related to PCE. Other metrics such as Voc and Jsc were not significantly affected. Series resistance often arises from the lower work energy function of electrodes and the number of layers in the Perovskite device.

The shunt resistance had the opposite effect on the performance of the Perovskite device. Performance characteristics increased when the shunt resistance was changed from 500 to 300

 doi:10.20944/preprints202406.0524.v1

Ohm.cm², but further increases did not yield any improvements. The enhancement in PCE and FF was a result of reducing pin-holes that typically diminish the performance of Perovskite devices

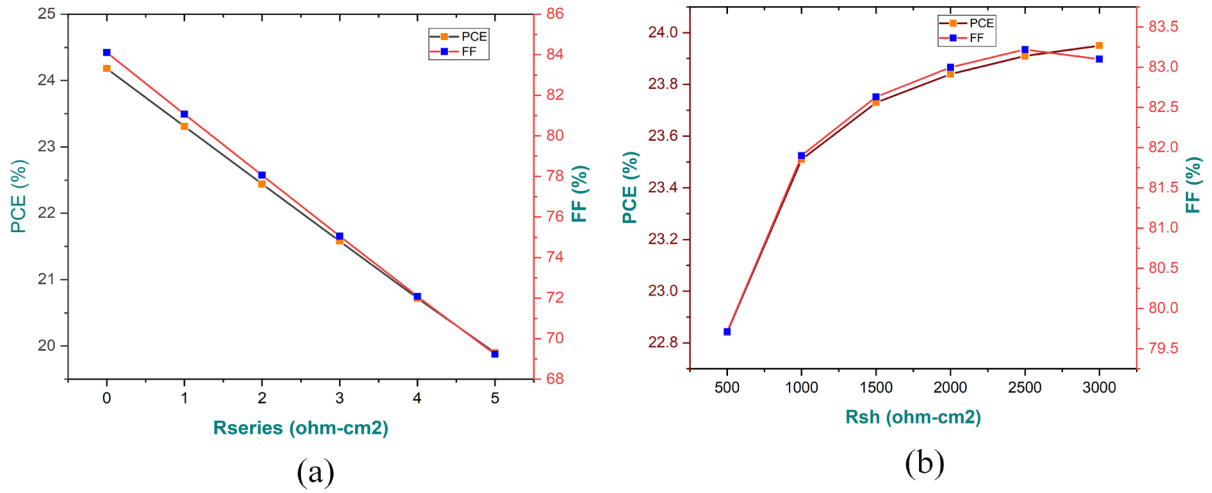

.

Figure 12. Impact of R_{series} and R_{sh} resistance on the performance parameters FF and PCE.

3.9. J-V Characteristics Analysis Curve

After meticulously adjusting all factors persuading the PCE and performance of the perovskite device, we conducted a J-V characteristics analysis to validate its electronic properties. The J-V characteristics curve is an essential tool for examining electrical output power and key performance parameters such as Voc, Jsc, and FF. The absorber layer was precisely tuned to an optimal thickness of 500 nm.

Operating at a temperature of 300 Kelvin, the system's output power was measured under standard testing conditions, using sunlight with a frequency of 106 Hz and an AM1.5G spectrum. The J-V characteristics curve provided optimal values for PCE and performance metrics. The final simulation results are presented below.

- Personal Consumption Expenditure at 24.18%
- Voltage of 0.928 V
- current density of 30.898 mA/cm2
- Fill factor of 84.39%

The reduced recombination rates—especially for Shock-ley-Read Hall recombination—as well as the anticipated recombination currents for the Perovskite device are depicted in Figure 13.

Preprints.org (www.preprints.org) | NOT PEER-REVIEWED | Posted: 11 June 2024 doi:10.20944/preprints202406.0524.v1

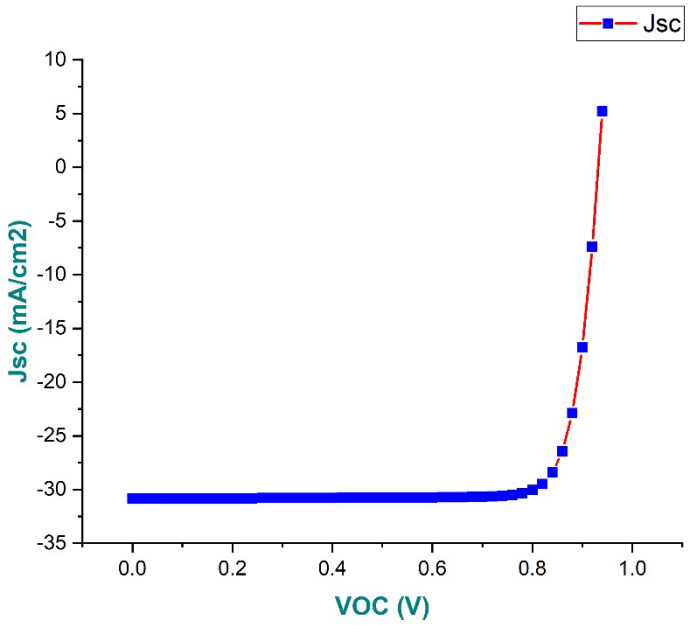

Figure 13. V-J characteristic curve of PSC .

3.10. Evaluation of the quantum Efficiency of Perovskite

Quantum efficiency serves as a vital measure for evaluating the performance of tin-based Perovskite materials. It quantifies the number of electrons generated when light, in the form of a photon beam, interacts with the Perovskite substance. Essentially, a higher rate of electron generation translates to a greater quantum efficiency for the device. Quantum efficiency can also be expressed concerning wavelength (nm) or photon energy.

To put it another way, the graph shows the link between wavelength (nm) and QE (%). Approximately 90% of the QE efficiency is found between 300 and 850 nm. This implies that there is a significant decrease in the recombination rate and a strong absorption capacity in the absorbent layer. In addition, quantum efficiency values calculated from photon energy are shown in Figures 14 and 15. These graphs show an increase in quantum efficiency levels between 1.8 and 3.2 eV of photon energy.

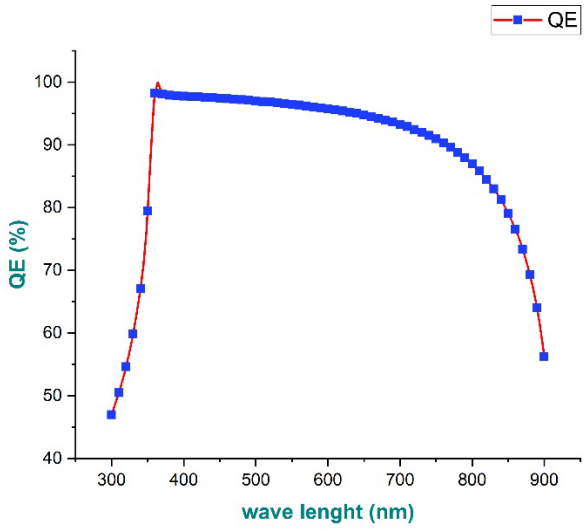

Figure 14. A relation between wavelength and quantum efficiency

 doi:10.20944/preprints202406.0524.v1

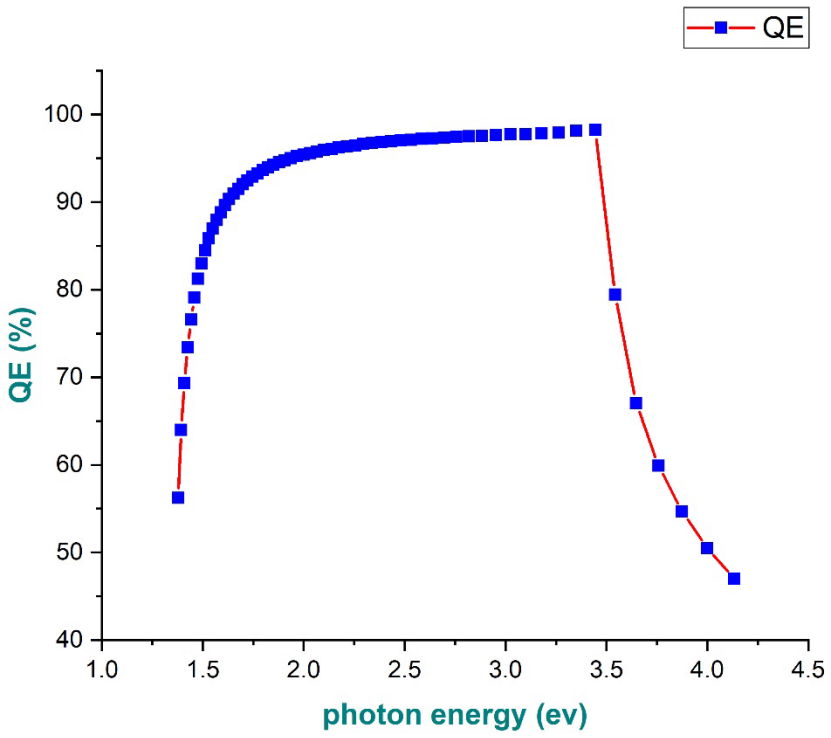

Figure 15. A relation between photon energy and quantum efficiency.

4. Conclusion

In conclusion, this study aimed to develop a high performance, cost-effective, and eco-friendly PSC based on lead-free tin. Utilizing the SCAPs-1D modeling tool, we designed and optimized a planar N-I-P architecture consisting of FTO/ZnO/$CH_3NH_3SnI_3$/CuSCN/Au layers. Through comprehensive numerical simulations and parametric analyses, we investigated the impact of various factors, including electron affinity, band gap, absorber layer thickness, doping concentration, and defect density, as well as shunt resistance, series resistance, and operating temperature, on Perovskite efficiency. Following meticulous optimization, the device exhibited a significant improvement, achieving a remarkable PCE of 24.18%, accompanied by enhanced performance parameters such as Voc of 0.9323V, Jsc of 30.8360 mA/cm^2, and FF of 84.10%. Notably, recombination rates, particularly Shockley-Read Hall recombination, were dramatically reduced. Despite the inherent drawbacks of planar topologies, we opted for a hole-carrying material (CuSCN) due to its superior carrier extraction capabilities compared to spiro-OMetad. Our simulation model not only increased PCE but also mitigated interfacial recombination, a common issue in Sn-based Perovskite materials. Additionally, incorporating a CuSCN transporting layer reduced interfacial defects by facilitating charge extraction and carrier transport. The study also highlighted the importance of optimizing front and back metal contacts, emphasizing the role of higher work energy function contacts in enhancing device performance by extracting more carriers from transporting layers. In summary, our findings suggest that by reducing interfacial and surface defects, optimizing absorber layer thickness, aligning band gaps, and selecting appropriate transporting materials and metal contacts, the performance of Sn-based PSCs can be significantly enhanced.

Acknowledgment: The authors extend their appreciation to King Saud University for funding this work through Researchers Supporting Project number (RSPD2024R685), King Saud University, Riyadh, Saudi Arabia.

References

1. Yao, L. New Energy Utilization in Environmental Design and Realization. *Energy Reports* **2022**, *8*, 9211–9220, doi:10.1016/J.EGYR.2022.07.029.

2. Kamran, M.; Fazal, M.R.; Mudassar, M.; Ahmed, S.R.; Adnan, M.; Abid, I.; Randhawa, F.J.S.; Shams, H. Solar Photovoltaic Grid Parity: A Review of Issues and Challenges and Status of Different PV Markets. *Int. J. Renew. Energy Res.* **2019**, *9*, 244–260, doi:10.20508/IJRER.V9I1.8933.G7580.
3. Shahid, H.; Kamran, M.; Mehmood, Z.; Saleem, M.Y.; Mudassar, M.; Haider, K. Implementation of the Novel Temperature Controller and Incremental Conductance MPPT Algorithm for Indoor Photovoltaic System. *Sol. Energy* **2018**, *163*, 235–242, doi:10.1016/J.SOLENER.2018.02.018.
4. Kamran, M.; Mudassar, M.; Fazal, M.R.; Asghar, M.U.; Bilal, M.; Asghar, R. Implementation of Improved Perturb & Observe MPPT Technique with Confined Search Space for Standalone Photovoltaic System. *J. King Saud Univ. - Eng. Sci.* **2020**, *32*, 432–441, doi:10.1016/j.jksues.2018.04.006.
5. Wang, J.; Xuan, Y.; Da, Y.; Xu, Y.; Zheng, L. Benefits of Photonic Management Strategy for Highly Efficient Bifacial Solar Cells. *Opt. Commun.* **2020**, *462*, 125358, doi:10.1016/J.OPTCOM.2020.125358.
6. Ashraf, M.; Ayaz, M.; Khan, M.; Adil, S.F.; Farooq, W.; Ullah, N.; Nawaz Tahir, M. Recent Trends in Sustainable Solar Energy Conversion Technologies: Mechanisms, Prospects, and Challenges. *Energy and Fuels* **2023**, *37*, 6283–6301, doi:10.1021/ACS.ENERGYFUELS.2C04077/ASSET/IMAGES/MEDIUM/EF2C04077_0006.GIF.
7. Hassan, Q.; Viktor, P.; J. Al-Musawi, T.; Mahmood Ali, B.; Algburi, S.; Alzoubi, H.M.; Khudhair Al-Jiboory, A.; Zuhair Sameen, A.; Salman, H.M.; Jaszczur, M. The Renewable Energy Role in the Global Energy Transformations. *Renew. Energy Focus* **2024**, *48*, 100545, doi:10.1016/J.REF.2024.100545.
8. Nie, T.; Fang, Z.; Ren, X.; Duan, Y.; Liu, S. (Frank) Recent Advances in Wide-Bandgap Organic–Inorganic Halide Perovskite Solar Cells and Tandem Application. *Nano-Micro Lett. 2023 151* **2023**, *15*, 1–44, doi:10.1007/S40820-023-01040-6.
9. Bati, A.S.R.; Zhong, Y.L.; Burn, P.L.; Nazeeruddin, M.K.; Shaw, P.E.; Batmunkh, M. Next-Generation Applications for Integrated Perovskite Solar Cells. *Commun. Mater. 2023 41* **2023**, *4*, 1–24, doi:10.1038/s43246-022-00325-4.
10. Kumari, N.; Patel, S.R.; Gohel, J. V. Optical and Structural Properties of ZnO Thin Films Prepared by Spray Pyrolysis for Enhanced Efficiency Perovskite Solar Cell Application. *Opt. Quantum Electron.* **2018**, *50*, doi:10.1007/S11082-018-1376-5.
11. Nykyruy, L.I.; Yavorskyi, R.S.; Zapukhlyak, Z.R.; Wisz, G.; Potera, P. Evaluation of CdS/CdTe Thin Film Solar Cells: SCAPS Thickness Simulation and Analysis of Optical Properties. *Opt. Mater. (Amst).* **2019**, *92*, 319–329, doi:10.1016/J.OPTMAT.2019.04.029.
12. Bimli, S.; Manjunath, V.; Mulani, S.R.; Miglani, A.; Game, O.S.; Devan, R.S. Theoretical Investigations of All Inorganic Cs2SnI6 Double Perovskite Solar Cells for Efficiency ~ 30 %. *Sol. Energy* **2023**, *256*, 76–87, doi:10.1016/J.SOLENER.2023.03.059.
13. Bati, A.S.R.; Sutanto, A.A.; Hao, M.; Batmunkh, M.; Yamauchi, Y.; Wang, L.; Wang, Y.; Nazeeruddin, M.K.; Shapter, J.G. Cesium-Doped Ti3C2Tx MXene for Efficient and Thermally Stable Perovskite Solar Cells. *Cell Rep. Phys. Sci.* **2021**, *2*, 100598, doi:10.1016/j.xcrp.2021.100598.
14. Bati, A.S.R.; Hao, M.; Macdonald, T.J.; Batmunkh, M.; Yamauchi, Y.; Wang, L.; Shapter, J.G. 1D-2D Synergistic MXene-Nanotubes Hybrids for Efficient Perovskite Solar Cells. *Small* **2021**, *17*, 2101925, doi:10.1002/smll.202101925.
15. Shaw, B.K.; Castillo-Blas, C.; Thorne, M.F.; Ríos Gómez, M.L.; Forrest, T.; Lopez, M.D.; Chater, P.A.; McHugh, L.N.; Keen, D.A.; Bennett, T.D. Principles of Melting in Hybrid Organic-Inorganic Perovskite and Polymorphic ABX3structures. *Chem. Sci.* **2022**, *13*, 2033–2042, doi:10.1039/D1SC07080K.
16. Wu, J.; Cha, H.; Du, T.; Dong, Y.; Xu, W.; Lin, C.T.; Durrant, J.R. A Comparison of Charge Carrier Dynamics in Organic and Perovskite Solar Cells. *Adv. Mater.* **2022**, *34*, 2101833, doi:10.1002/adma.202101833.
17. Bati, A.S.R.; Yu, L.P.; Tawfik, S.A.; Spencer, M.J.S.; Shaw, P.E.; Batmunkh, M.; Shapter, J.G. Electrically Sorted Single-Walled Carbon Nanotubes-Based Electron Transporting Layers for Perovskite Solar Cells. *iScience* **2019**, *14*, 100–112, doi:10.1016/j.isci.2019.03.015.
18. Zhang, Y.; Kirs, A.; Ambroz, F.; Lin, C.T.; Bati, A.S.R.; Parkin, I.P.; Shapter, J.G.; Batmunkh, M.; Macdonald, T.J. Ambient Fabrication of Organic–Inorganic Hybrid Perovskite Solar Cells. *Small Methods* **2021**, *5*, 2000744, doi:10.1002/smtd.202000744.
19. Park, H.-J.; Son, H.; Jeong, B.-S. SCAPS-1D Simulation for Device Optimization to Improve Efficiency in Lead-Free CsSnI3 Perovskite Solar Cells. *Inorganics 2024, Vol. 12, Page 123* **2024**, *12*, 123, doi:10.3390/INORGANICS12040123.
20. Jung, H.S.; Han, G.S.; Park, N.G.; Ko, M.J. Flexible Perovskite Solar Cells. *Joule* **2019**, *3*, 1850–1880, doi:10.1016/J.JOULE.2019.07.023.
21. Goetz, K.P.; Taylor, A.D.; Hofstetter, Y.J.; Vaynzof, Y. Sustainability in Perovskite Solar Cells. *ACS Appl. Mater. Interfaces* **2021**, *13*, 1–17, doi:10.1021/ACSAMI.0C17269.
22. Liu, B.; Long, M.; Cai, M.Q.; Yang, J. Influence of the Number of Layers on Ultrathin CsSnI3 Perovskite: From Electronic Structure to Carrier Mobility. *J. Phys. D. Appl. Phys.* **2018**, *51*, doi:10.1088/1361-6463/AAA7CA.

23. Gamal, N.; Sedky, S.H.; Shaker, A.; Fedawy, M. Design of Lead-Free Perovskite Solar Cell Using Zn1-XMgxO as ETL: SCAPS Device Simulation. *Optik (Stuttg).* **2021**, *242*, doi:10.1016/J.IJLEO.2021.167306.
24. Liu, C.; Li, W.; Zhang, C.; Ma, Y.; Fan, J.; Mai, Y. All-Inorganic CsPbI2Br Perovskite Solar Cells with High Efficiency Exceeding 13%. *J. Am. Chem. Soc.* **2018**, *140*, 3825–3828, doi:10.1021/JACS.7B13229.
25. Giustino, F.; Snaith, H.J. Toward Lead-Free Perovskite Solar Cells. *ACS Energy Lett.* **2016**, *1*, 1233–1240, doi:10.1021/ACSENERGYLETT.6B00499.
26. Cao, J.; Yan, F. Recent Progress in Tin-Based Perovskite Solar Cells. *Energy Environ. Sci.* **2021**, *14*, 1286–1325, doi:10.1039/D0EE04007J.
27. Montecucco, R.; Quadrivi, E.; Po, R.; Grancini, G. All-Inorganic Cesium-Based Hybrid Perovskites for Efficient and Stable Solar Cells and Modules. *Adv. Energy Mater.* **2021**, *11*, doi:10.1002/AENM.202100672.
28. Li, B.; Di, H.; Chang, B.; Yin, R.; Fu, L.; Zhang, Y.N.; Yin, L. Efficient Passivation Strategy on Sn Related Defects for High Performance All-Inorganic CsSnI3 Perovskite Solar Cells. *Adv. Funct. Mater.* **2021**, *31*, doi:10.1002/ADFM.202007447.
29. Chen, H.; Xiang, S.; Li, W.; Liu, H.; Zhu, L.; Yang, S. Inorganic Perovskite Solar Cells: A Rapidly Growing Field. *Sol. RRL* **2018**, *2*, doi:10.1002/SOLR.201700188.
30. Roy, P.; Sinha, N.K.; Tiwari, S.; Khare, A. Influence of Defect Density and Layer Thickness of Absorption Layer on the Performance of Tin Based Perovskite Solar Cell. *IOP Conf. Ser. Mater. Sci. Eng.* **2020**, *798*, doi:10.1088/1757-899X/798/1/012020.
31. Hossain, M.K.; Toki, G.F.I.; Kuddus, A.; Mohammed, M.K.A.; Pandey, R.; Madan, J.; Bhattarai, S.; Rahman, M.F.; Dwivedi, D.K.; Amami, M.; et al. Optimization of the Architecture of Lead-Free CsSnCl3-Perovskite Solar Cells for Enhancement of Efficiency: A Combination of SCAPS-1D and WxAMPS Study. *Mater. Chem. Phys.* **2023**, *308*, doi:10.1016/J.MATCHEMPHYS.2023.128281.
32. Wang, N.; Zhou, Y.; Ju, M.G.; Garces, H.F.; Ding, T.; Pang, S.; Zeng, X.C.; Padture, N.P.; Sun, X.W. Heterojunction-Depleted Lead-Free Perovskite Solar Cells with Coarse-Grained B-γ-CsSnI3 Thin Films. *Adv. Energy Mater.* **2016**, *6*, doi:10.1002/AENM.201601130.
33. Lin, S.; Zhang, B.; Lü, T.Y.; Zheng, J.C.; Pan, H.; Chen, H.; Lin, C.; Li, X.; Zhou, J. Inorganic Lead-Free B-γ-CsSnI3Perovskite Solar Cells Using Diverse Electron-Transporting Materials: A Simulation Study. *ACS Omega* **2021**, *6*, 26689–26698, doi:10.1021/ACSOMEGA.1C04096.
34. Petrus, M.L.; Schlipf, J.; Li, C.; Gujar, T.P.; Giesbrecht, N.; Müller-Buschbaum, P.; Thelakkat, M.; Bein, T.; Hüttner, S.; Docampo, P. Capturing the Sun: A Review of the Challenges and Perspectives of Perovskite Solar Cells. *Adv. Energy Mater.* **2017**, *7*, doi:10.1002/AENM.201700264.
35. Li, Z.; Wang, R.; Xue, J.; Xing, X.; Yu, C.; Huang, T.; Chu, J.; Wang, K.L.; Dong, C.; Wei, Z.; et al. Core-Shell ZnO@SnO2 Nanoparticles for Efficient Inorganic Perovskite Solar Cells. *J. Am. Chem. Soc.* **2019**, *141*, 17610–17616, doi:10.1021/JACS.9B06796.
36. Dunfield, S.P.; Bliss, L.; Zhang, F.; Luther, J.M.; Zhu, K.; van Hest, M.F.A.M.; Reese, M.O.; Berry, J.J. From Defects to Degradation: A Mechanistic Understanding of Degradation in Perovskite Solar Cell Devices and Modules. *Adv. Energy Mater.* **2020**, *10*, doi:10.1002/AENM.201904054.
37. Moustafa, M.; Alzoubi, T. Numerical Simulation of Single Junction Ingan Solar Cell by Scaps. *Key Eng. Mater.* **2019**, *821 KEM*, 407–413, doi:10.4028/WWW.SCIENTIFIC.NET/KEM.821.407.
38. Zhang, J.; Hodes, G.; Jin, Z.; Liu, S. All-Inorganic CsPbX3 Perovskite Solar Cells: Progress and Prospects. *Angew. Chemie - Int. Ed.* **2019**, *58*, 15596–15618, doi:10.1002/ANIE.201901081.
39. Fatima, Q.; Haidry, A.A.; Hussain, R.; Zhang, H. Device Simulation of a Thin-Layer CsSnI3-Based Solar Cell with Enhanced 31.09% Efficiency. *Energy and Fuels* **2023**, *37*, 7411–7423, doi:10.1021/ACS.ENERGYFUELS.3C00645.
40. Ansari, M.I.H.; Qurashi, A.; Nazeeruddin, M.K. Frontiers, Opportunities, and Challenges in Perovskite Solar Cells: A Critical Review. *J. Photochem. Photobiol. C Photochem. Rev.* **2018**, *35*, 1–24, doi:10.1016/J.JPHOTOCHEMREV.2017.11.002.